

Effects of tunable hydrophobicity on the collective hydrodynamics of Janus particles under flows

Szu-Pei Fu ¹, Rolf Ryham ², Bryan Quaife ³ and Y.-N. Young ⁴

¹*Department of Mathematics, Trinity College, Hartford, Connecticut 06106, USA*

²*Department of Mathematics, Fordham University, Bronx, New York 10458, USA*

³*Department of Scientific Computing, Florida State University, Tallahassee, Florida 32306, USA*

⁴*Department of Mathematical Sciences, New Jersey Institute of Technology, Newark, New Jersey 07102, USA*



(Received 5 August 2022; accepted 14 April 2023; published 11 May 2023)

Active colloidal systems with nonequilibrium self-organization constitute a long-standing, challenging area in material sciences and biology. To understand how hydrodynamic flow may be used to actively control self-assembly of Janus particles (JPs), we developed a model for the many-body hydrodynamics of amphiphilic JPs suspended in a viscous fluid with imposed far-field background flows [Fu *et al.*, *J. Fluid Mech.* **941**, A41 (2022)]. In this paper we alter the hydrophobic distribution on the JP-solvent interface to investigate the hydrodynamics that underlies the various morphologies and rheological properties of the JP assembly in the suspension. We find that JPs assemble into unilamellar, multilamellar, and striated structures. To introduce dynamics, we include a planar linear shear flow and a steady Taylor-Green mixing flow and measure the collective dynamics of JP particles in terms of their (a) free energy from the hydrophobic interactions between the JPs, (b) order parameter for the ordering of JPs in terms of alignment of their directors, and (c) strain parameter that captures the deformation in the assembly. We characterize the effective material properties of the JP structures and find that the unilamellar structure increases orientation order under shear flow, the multilamellar structure behaves as a shear thinning fluid, and the striated structure possesses a yield stress. These numerical results provide insights into dynamic control of nonequilibrium active biological systems with similar self-organization.

DOI: [10.1103/PhysRevFluids.8.050501](https://doi.org/10.1103/PhysRevFluids.8.050501)

I. INTRODUCTION

Janus particles (JPs) are colloids with dissimilar chemical or physical functionalities between the two sides of their surfaces [1,2]. Self-propelling JPs, for example, with a permanent biphasic asymmetry, have emerged as a rich chemical platform for the exploration of active matter [3] and mobility-induced phase separation. In the absence of mobility and any imposed flow, JPs self-assemble into oligomers of various geometries and sizes depending on the interactions between JPs and the viscous solvent [4–6], with tunable functions for biomedical engineering applications [2,7–11].

When driven by an external flow, dynamic rearrangement of JPs emerges naturally from the interactions between particles and fluid in colloidal matter [12]. Such colloidal hydrodynamics belong to a wide class of nonequilibrium self-organization in physics, often with complexity and features similar to that of biological systems such as living cells, bacterial baths, and animal flocks [13,14]. A long-standing challenge in fluid mechanics and material science is to solve the “inverse” problem of creating a model colloidal system that will self-assemble into prescribed structures [15]. For example, the framework of geometrical frustration, which has been used to explain disordered

systems, could instead be used to design new, ordered systems, through specific choices for the shapes or interactions of the particles [16].

In this paper we focus on collective hydrodynamics of immobile (non-self-propelling) JPs in a viscous fluid under an imposed far-field flow. The amphiphilic JP has a hydrophobic surface on one side and a hydrophilic surface on the other side [17]. The many-body hydrodynamics of amphiphilic Janus particles assembled as vesicles (self-enclosed bilayers of JPs) suspended in a viscous fluid in the inertialess regime (zero Reynolds number) has been studied using boundary integral numerical simulations [18,19]. The dynamics of the JP suspension arises spontaneously from the combination of long-range hydrodynamic interaction and nonlocal interactions between JPs through the distribution of a hydrophobic attraction potential (HAP). In a quiescent flow, an amphiphilic JP suspension self-assembles into micelles and bilayers of JPs that provide an alternative means for computing the mechanical moduli of a colloidal membrane in numerical simulations [18,20,21]. Under background flows, the hydrodynamics of a JP vesicle (a self-enclosed bilayer of JPs) exhibit many familiar behaviors of a vesicle: elongation and alignment along the extensional direction, tank-treading, and rupture of a vesicle under shear flow [19,22–26].

Molecular dynamics (MD) and Monte Carlo simulations provide another means for simulating the interaction between amphiphilic JPs, solvents, and substrates [6,27–29]. In these methods, pair potentials are used to describe the interaction between amphiphilic JPs by prescribing angle-dependent forces and torques that bring the hydrophobic sides of two amphiphilic JPs into opposition. On the other hand, the HAP formulation in this paper has attractive, long-range forces and torques, and they are instead derived from a boundary value problem for the molecular structure of water [30–34]. Unlike in MD or Monte Carlo simulations, the HAP interactions are nonadditive [18], so that the interactions between a pair of JPs are affected by the presence of other particles. As such, the HAP is a phase-field function that represents the properties of the solvent in the presence of JPs. Such an approach falls into the category of work that considers particles as a discretization of a continuum problem [35].

Here we take advantage of the flexibility of the HAP model to examine the effects of tuning the distribution of hydrophobicity on JP surfaces. Such variation of the boundary condition on JP surfaces has been realized experimentally by using chemicals to adjust the polarity of the viscous solvent [2,11,17]. We show that a simple tuning of the hydrophobic distribution leads to transitions from unilamellar to multilamellar or striated superstructures of JPs. Focusing on the fluid-structure interactions that correspond to such transitions, we investigate the deformation of these novel structures in background flows and map out their collective behavior away from equilibrium. Looking forward, including other fields such as electric potential for JPs synthesized with charged polymers [5,6,17] is straightforward within the context of the boundary integral representations [36], opening further lines of investigation.

This paper is organized as follows. Section II summarizes the general mathematical formulation. Section III describes the three types of hydrophobicity distribution that we use in the numerical simulations. Section IV outlines the quantitative measures used to describe the collective hydrodynamics of JPs summarized and discussed in Sec. V. Finally, Sec. VI provides a conclusion and a discussion of future directions.

II. GOVERNING EQUATIONS: HYDROPHOBIC ATTRACTION POTENTIAL MOBILITY PROBLEM

The governing equations are a system of partial differential equations for the position and orientation of a collection of rigid JPs [19]. We first pose the Stokes equations for the mobility problem giving the hydrodynamic interactions for the particle suspension. The hydrophobic forces come from solving a screened Laplace equation. Particle collisions are avoided through a near-field, pair potential for their steric interactions.

A. Mobility problem

The JPs are disks of radius c suspended in a viscous solvent with center \mathbf{a}_i and orientation θ_i relative to the horizontal axis, where $i = 1, \dots, N_b$, and N_b is the number of particles. The domain $\Omega \subset \mathbb{R}^2$ is the solvent phase and t is time. The boundary of Ω is $\partial\Omega = \Gamma_1 \cup \dots \cup \Gamma_{N_b}$, where Γ_i is the boundary of Janus particle i . The sets Ω , Γ_1, \dots , and Γ_{N_b} depend on t . Assuming that inertial terms are negligible, the solvent satisfies the Stokes equations

$$-\mu \Delta \mathbf{u} + \nabla p = \mathbf{0}, \quad \mathbf{x} \in \Omega, \quad (1)$$

$$\nabla \cdot \mathbf{u} = 0, \quad \mathbf{x} \in \Omega, \quad (2)$$

$$\mathbf{u} - \mathbf{u}_\infty \rightarrow \mathbf{0}, \quad |\mathbf{x}| \rightarrow \infty, \quad (3)$$

where \mathbf{u} is the velocity, p is the pressure, \mathbf{u}_∞ is the background flow velocity, and μ is the constant solvent viscosity. The solvent velocity satisfies the no-slip boundary condition for a rigid body motion

$$\mathbf{u}(\mathbf{x}) = \mathbf{v}_i + \omega_i(\mathbf{x} - \mathbf{a}_i)^\perp, \quad \mathbf{x} \in \Gamma_i, \quad (4)$$

where \mathbf{v}_i is the translational velocity, ω_i is the angular velocity, and $\langle x, y \rangle^\perp = \langle -y, x \rangle$.

To obtain forces, define the free energy [18,19]

$$F = \gamma \int_{\Omega} (\rho |\nabla u|^2 + \rho^{-1} u^2) d\mathbf{x} + \frac{M}{2} \sum_{j \neq i} P\left(\frac{|\mathbf{a}_i - \mathbf{a}_j| - 2c}{\rho_0}\right), \quad (5)$$

where $u(\mathbf{x}, t)$ is the order parameter for water [30,31], ρ is a decay length, and γ is an interfacial tension. The order parameter $u(\mathbf{x}, t)$ is assumed to minimize the free energy F and therefore satisfies the screened Laplace boundary value problem

$$-\rho^2 \Delta u + u = 0, \quad \mathbf{x} \in \Omega, \quad (6)$$

$$u = g, \quad \mathbf{x} \in \partial\Omega, \quad u \rightarrow 0, \quad |\mathbf{x}| \rightarrow \infty. \quad (7)$$

The boundary condition g encodes hydrophobic properties of the particle-solvent interface. The dimensionless repulsion profile takes the form $P(s) = 1 - \sin(\pi s/2)$ for $0 \leq s < 1$ and $P(s) = 0$ for $s \geq 1$. The parameter ρ_0 is the distance below which steric repulsion becomes important, and M is the repulsion modulus.

Letting \mathbf{v} be the particle outward normal, the force \mathbf{F}_i and torque T_i coming from the free energy acting on Γ_i are [18]

$$\mathbf{F}_i = \int_{\Gamma_i} \mathbf{T} \mathbf{v} ds - \frac{M}{\rho_0} \sum_{j \neq i} \frac{\mathbf{a}_i - \mathbf{a}_j}{|\mathbf{a}_i - \mathbf{a}_j|} P'\left(\frac{|\mathbf{a}_i - \mathbf{a}_j| - 2c}{\rho_0}\right), \quad T_i = \int_{\Gamma_i} (\mathbf{x} - \mathbf{a}_i)^\perp \cdot (\mathbf{T} \mathbf{v}) ds. \quad (8)$$

Here,

$$\mathbf{T} = \gamma [\rho^{-1} u^2 \mathbf{I} + \rho (|\nabla u|^2 \mathbf{I} - 2 \nabla u \nabla u^T)] \quad (9)$$

is the second-order hydrophobic stress tensor. Repulsion is rotationally symmetric and does not enter T_i .

Without inertia, (\mathbf{u}, p) satisfy the force-free and torque-free conditions, meaning that the force and torque from the hydrodynamic stress on each particle balance the total force and torque coming from the hydrophobic potential and repulsion. We have

$$\int_{\Gamma_i} \boldsymbol{\sigma} \cdot \mathbf{v} ds = \mathbf{F}_i, \quad \int_{\Gamma_i} (\mathbf{x} - \mathbf{a}_i)^\perp \cdot (\boldsymbol{\sigma} \cdot \mathbf{v}) ds = T_i, \quad i = 1, \dots, N_b, \quad (10)$$

where $\boldsymbol{\sigma} = -p \mathbf{I} + \mu (\nabla \mathbf{u} + \nabla \mathbf{u}^T)$ is the hydrodynamic stress tensor.

To perform a single time step, we (i) solve (6) and (7) for u , (ii) compute the force and torque (8), and (iii) solve the Stokes equations (1)–(3) subject to (4) and (10). The velocities (\mathbf{v}_i, ω_i) obtained from (4) are used to update the particle positions and orientations using the second-order Adams-Bashforth scheme with time step size Δt .

The interactions generated by the HAP mobility problem formulation (1)–(10) lead to particle self-assembly. In terms of scaling, ρ sets the effective distance of the hydrophobic interactions; ρ_0 determines the distance where attraction and repulsion are in balance, i.e., smaller values of ρ_0 lead to more compact particle assemblies. The rate of self-assembly is proportional to tension γ , inversely proportional to viscosity μ , and approximately inversely proportional to ρ [18].

B. Boundary integral representations

We require a method to accurately solve the Stokes and screened Laplace equations in intricate, unbounded geometries. This is done by recasting Eqs. (1)–(4) and Eqs. (6) and (7) as boundary integral equations (BIEs) and discretizing each BIE at N points on each of the N_b particles with a collocation method. To express the solution of (6) and (7), we adopt the double-layer potential

$$u(\mathbf{x}) = \mathcal{D}[\sigma](\mathbf{x}) = \int_{\partial\Omega} \frac{\partial G(\mathbf{x} - \mathbf{y})}{\partial \mathbf{v}_y} \eta(\mathbf{y}) ds_y, \quad \mathbf{x} \in \Omega, \quad (11)$$

where $G(\mathbf{x}) = \frac{1}{2\pi} K_0(|\mathbf{x}|/\rho)$ is the fundamental solution of the screened Laplace equation (6), K_0 is the zeroth-order modified Bessel function of the second kind, \mathbf{v}_y is the unit outward normal at \mathbf{y} , and η is a scalar-valued density function. The subscript in ds_y denotes integration with respect to $\mathbf{y} \in \partial\Omega$. To satisfy the boundary condition (7), the density function must satisfy [37]

$$g(\mathbf{x}) = \frac{1}{2} \eta(\mathbf{x}) + \mathcal{D}[\eta](\mathbf{x}), \quad \mathbf{x} \in \partial\Omega. \quad (12)$$

For the velocity, we use the completed double-layer potential representation [38]

$$\mathbf{u}(\mathbf{x}) = \mathbf{u}_\infty(\mathbf{x}) + \mathcal{D}[\boldsymbol{\eta}](\mathbf{x}) + \sum_{i=1}^{N_b} (\mathbf{S}(\mathbf{x}, \mathbf{a}_i) \cdot \mathbf{F}_i + \mathbf{R}(\mathbf{x}, \mathbf{a}_i) T_i), \quad \mathbf{x} \in \Omega, \quad (13)$$

where $\boldsymbol{\eta}$ is a vector-valued density function and

$$\mathcal{D}[\boldsymbol{\eta}](\mathbf{x}) = \frac{1}{\pi} \int_{\Gamma} \frac{(\mathbf{x} - \mathbf{y}) \cdot \mathbf{v}_y}{|\mathbf{x} - \mathbf{y}|^2} \frac{(\mathbf{x} - \mathbf{y}) \otimes (\mathbf{x} - \mathbf{y})}{|\mathbf{x} - \mathbf{y}|^2} \cdot \boldsymbol{\eta}(\mathbf{y}) ds_y. \quad (14)$$

The Stokeslets and Rotlets are

$$\mathbf{S}(\mathbf{x}, \mathbf{a}_i) = \frac{1}{4\pi} \left(-\ln |\mathbf{r}| \mathbf{I} + \frac{\mathbf{r} \otimes \mathbf{r}}{|\mathbf{r}|^2} \right), \quad \mathbf{R}(\mathbf{x}, \mathbf{a}_i) = \frac{1}{4\pi} \frac{\mathbf{r}^\perp}{|\mathbf{r}|^2}, \quad (15)$$

respectively, where $\mathbf{r} = \mathbf{x} - \mathbf{a}_i$. Letting \mathbf{x} approach Γ_i in (13), applying the jump condition of the double-layer potential [39], and imposing the no-slip boundary condition (4), the density function $\boldsymbol{\eta}$, translational velocity \mathbf{v}_i , and rotational velocity ω_i satisfy

$$\mathbf{v}_i + \omega_i (\mathbf{x} - \mathbf{a}_i)^\perp = \mathbf{u}_\infty(\mathbf{x}) - \frac{1}{2} \boldsymbol{\eta}(\mathbf{x}) + \mathcal{D}[\boldsymbol{\eta}](\mathbf{x}) + \sum_{j=1}^{N_b} (\mathbf{S}(\mathbf{x}, \mathbf{a}_j) \cdot \mathbf{F}_j + \mathbf{R}(\mathbf{x}, \mathbf{a}_j) T_j), \quad (16)$$

$$\int_{\Gamma_i} \boldsymbol{\eta} ds = \mathbf{F}_i, \quad \int_{\Gamma_i} \boldsymbol{\eta} \cdot (\mathbf{x} - \mathbf{a}_i)^\perp ds = T_i, \quad (17)$$

for $\mathbf{x} \in \Gamma_i$ and $i = 1, \dots, N_b$. Alternative full-rank layer potential representations for rigid body motions are possible [40,41].

We discretize Eq. (12) and Eqs. (16) and (17) using high-order interpolation-based quadrature rules. Smooth integrals are computed with the spectrally accurate trapezoid rule, and nearly

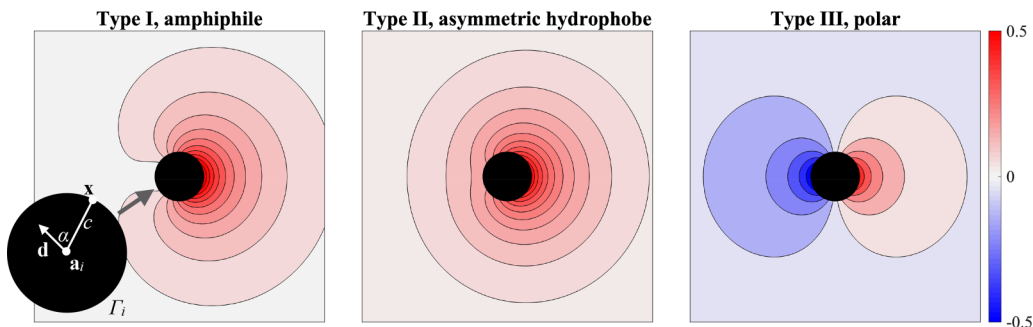


FIG. 1. The leftmost diagram illustrates the particle Γ_i with center \mathbf{a}_i , radius c , and director \mathbf{d} , along with the angle α . The three rightmost panels plots show $g(\mathbf{x})$ and the respective solutions $u(\mathbf{x})$ of (6) for an isolated particle.

singular integrals, caused by close contact between two particles, are computed with a high-order interpolation-based quadrature rule [42].

After discretizing and applying quadrature, the result is an $NN_b \times NN_b$ linear system and a $(2N + 3)N_b \times (2N + 3)N_b$ linear system for Eq. (12) and for Eqs. (16) and (17), respectively. These are solved with the matrix-free generalized minimal residual method (GMRES), and the second-kind nature of the BIEs guarantees that the number of GMRES iterations is mesh independent.

III. TUNABLE HYDROPHOBICITY

The parameters are modeled after those for phospholipid in water [43]. We use $\mu = 1$ mPa s for the viscosity of water at room temperature. Pure lipid components give a range of interfacial tensions [44–47] 0.7–5.3 pN/nm. We use $\gamma = 4.1$ pN/nm, which gives a physically reasonable elastic modulus κ of lipid bilayers [18,19]. The particle radius $c = 1.25$ nm represents one-half of phospholipid length [43], and the screening length $\rho = 5$ nm derives from experimental force-distance measurements of hydrophobic attraction [32–34,46]. A repulsion modulus $M = 2$ pN and distance $\rho_0 = 0.5$ nm gives an interparticle distance around one particle radius, ensuring the accuracy of the boundary integral representations (11) and (13) without overly aggressive mesh refinement. The characteristic time and length are 1 ns and 1 nm, respectively.

Boundary conditions and equilibrium configurations

The boundary condition $g(\mathbf{x})$ in (7) defines the spatial distribution of hydrophobicity and hydrophilicity. Referring to Fig. 1, we let

$$g(\mathbf{x}) = a(b + \cos \alpha), \quad a = (\pi c(2b^2 + 1))^{-1/2}, \quad \mathbf{x} \in \Gamma_i, \quad (18)$$

where α is the angle between the vector $\mathbf{x} - \mathbf{a}_i$ and the particle director $\mathbf{d}_i = (\cos \theta_i, \sin \theta_i)$. The scalar b shifts the periodic date up and down, and the scalar a normalizes g so that $\int_{\Gamma_i} g^2(\mathbf{x}) ds = 1$. The side of the particle where $\alpha = 0$ is called the tail, and the side where $\alpha = \pi$ is the head.

Based on the choice of b , the boundary condition (BC) (18) can be classified into one of three categories: type I, amphiphile, $b = 1$, g is positive on one side representing a hydrocarbon-water interface and is zero on the other representing an apolar, hydrophilic region; type II, asymmetric hydrophobe, $b = 2$, g is positive on both sides but more so on one side; and type III, polar, $b = 0$, g is positive on one side and negative on the other, representing a water structure with positive and negative charge [30,48].

Figure 2 shows the steady state in a quiescent flow. Three distinct phases emerge. For type I, amphiphiles, the tail interactions are attractive, and particles collectively form disjoint bilayer components [Fig. 2(b)]. We refer to this as the “bilayer” phase.

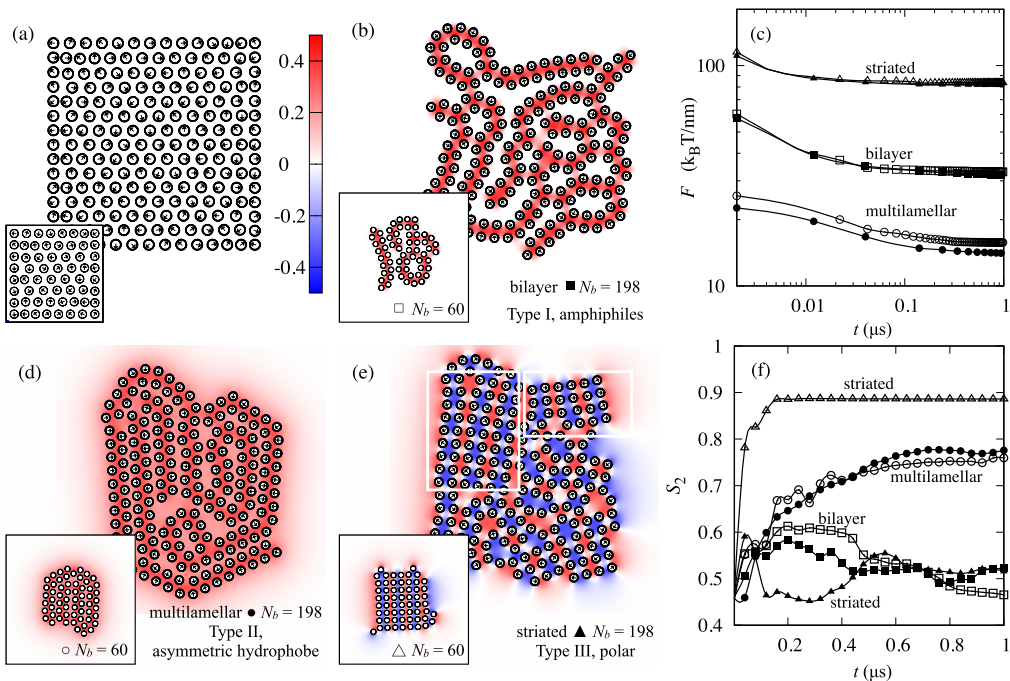


FIG. 2. (a) shows the $t = 0$, $N_b = 198$ particle configuration with random orientation and initially confined to a box. (b), (d), and (e) show bilayer, multilamellar, and striated phases composed of amphiphilic (type I), asymmetric hydrophobe (type II), and polar (type III) JPs, respectively. (c) and (f) plot the free energies (5) and alignment order parameter (22) with respect to t . The open symbols in (c) are for $N_b = 60$, and the solid symbols are for $N_b = 198$ but normalized by $60/198$, showing that the energy approximately scales with the number of particles. Alignment in the striated phase is particle number dependent; see triangle symbols in (f).

For type II, asymmetric hydrophobes, both sides of the JP are hydrophobic but more so on the tail. Over short times, these particles self-assemble into bilayers. However, unlike for type I JPs, the heads are also hydrophobic, and so over long times, the bilayers sort into a “multilamellar” phase. The number of layers depends on the number of particles. Figure 2(d), for example, shows a multilamellar structure with four layers and one with two layers in the inset. Onionlike dendrimersomes have previously been studied by molecular dynamics simulations using an anisotropic pair potential [6,29].

Finally, type III, bipolar JPs possess a head that repels the tail of neighboring particles. These JPs initially form chains with their directors perpendicular to the length of the chain. The chains form stria where the particles lie on a square grid and the orientations alternate between layers [Fig. 2(e)]. We refer to this as the “striated” phase.

See Sec. S1 of the Supplemental Material for movies showing the transition of 60 JPs that are initialized randomly [inset of Fig. 2(a)] to the steady-state configurations [insets of Figs. 2(b), 2(d), and 2(e)] [49].

IV. MEASURING DEFORMATION

To quantify the hydrodynamics of JP phases, we use the free energy F , a strain parameter E , and a scalar order parameter S_2 for alignment. First we simplify the form of the free energy (5). Using

integration by parts and (6), we obtain

$$F = -\gamma \int_{\partial\Omega} \rho g \nabla u \cdot \mathbf{v} ds + \frac{M}{2} \sum_{j \neq i} P \left(\frac{|\mathbf{a}_i - \mathbf{a}_j| - 2c}{\rho_0} \right). \quad (19)$$

Here, we have substituted g for u since the boundary values are given. However, evaluating $\nabla u \cdot \mathbf{v}$ on $\partial\Omega$ based on (11) involves calculating a gradient of a double-layer potential which has a well-known obstacle in numerical implementation. The Appendix describes how we overcome this obstacle.

Figure 2(c) tracks the free-energy profiles for all relaxation runs. In quiescent background flow, the energies are decreasing with respect to t showing that time stepping correctly accounts for viscous dissipation. Furthermore, the normalized energy plots provide evidence that the free energy per particle with specified boundary condition is independent of the total particle number N_b .

To measure positional order, we introduce the strain parameter,

$$E = \frac{1}{N_b} \sum_{i=1}^{N_b} \left\| \frac{1}{2} (\mathbf{F}_i^T \mathbf{F}_i - I) \right\|, \quad (20)$$

where \mathbf{F}_i is an approximate deformation gradient and $\|\cdot\|$ is the Frobenius norm. The Green-Lagrange strain tensor $\frac{1}{2}(\mathbf{F}_i^T \mathbf{F}_i - I)$ measures departure of fluid deformations from a rigid body motion. To define \mathbf{F}_i , we solve the overdetermined system

$$\mathbf{a}_j(t) - \mathbf{a}_i(t) = \mathbf{F}_i(\mathbf{a}_j(0) - \mathbf{a}_i(0)), \quad j = 1, \dots, N_b, \quad (21)$$

for \mathbf{F}_i by weighted least squares. That way, if the particle positions are given by a map $\mathbf{f}(\mathbf{a}_i(0), t) = \mathbf{a}_i(t)$, then $\mathbf{F}_i \approx \nabla \mathbf{f}(\mathbf{a}_i(0), t)$. The weights $w_i = \exp(-\|\mathbf{a}_j(0) - \mathbf{a}_i(0)\|/4c)$ with particle radius c ensure that the linear approximation holds for particles near \mathbf{a}_i .

Finally, we use the scalar order parameter S_2 to quantify the orientational order [50]:

$$S_2 = \frac{1}{N_b} \sum_{i=1}^{N_b} \frac{1}{2} (3 \cos^2(\theta_i - \bar{\theta}) - 1). \quad (22)$$

Here, $\bar{\theta}_i$ is a circular mean defined as the orientation of the principal eigenvector of the matrix $\sum_j \mathbf{d}_j \mathbf{d}_j^T$ where j runs over the particles whose centers lie within $4c$ of that of particle i . Defined as such, S_2 lies in the range $-1/2 \leq S_2 \leq 1$ with a value $S_2 = 1$ indicating perfect alignment between particles while $S_2 = -1/2$ indicates isotropic alignment locally. The cutoff distance $4c$ was chosen empirically so that the average includes nearest neighbors but excludes next-nearest neighbors.

In Fig. 2(f), the multilamellar phase is highly ordered whereas the bilayer phase is somewhat disordered because it consists of several components forming isolated bilayers, micelles, and vesicles [Fig. 2(b)].

The striated phase order admits more than one pattern depending on the number of particles [Fig. 2(f), triangles]. When the number of particles is small, there is only a single pattern where the directors are more or less parallel and alternate directions [Fig. 2(e), inset]. A larger number of particles results in multiple alignment patterns: the alternating sign pattern as in the small-particle-number case [Fig. 2(e), top right rectangle] and an X-shaped alignment [Fig. 2(e), top left rectangle].

V. RESULTS AND DISCUSSION

We subject the type I, II, and III JP phases to background flows and measure their material response. The background flows are a shear flow

$$\mathbf{u}_\infty^{\text{sh}}(\mathbf{x}) = \dot{\gamma}(\mathbf{e}_y \cdot \mathbf{x})\mathbf{e}_x \quad (23)$$

and a Taylor-Green (TG) flow

$$\mathbf{u}_\infty^{\text{TG}}(\mathbf{x}) = \lambda \dot{\gamma} (-\cos(\mathbf{e}_x \cdot \mathbf{x}/\lambda) \sin(\mathbf{e}_y \cdot \mathbf{x}/\lambda)\mathbf{e}_x + \sin(\mathbf{e}_x \cdot \mathbf{x}/\lambda) \cos(\mathbf{e}_y \cdot \mathbf{x}/\lambda)\mathbf{e}_y), \quad (24)$$

where the orthonormal vectors \mathbf{e}_x and \mathbf{e}_y are the horizontal and vertical directions, respectively. The shear flow replicates the motion of a fluid between two parallel, moving plates excluding wall effects. In TG flow, λ controls the size of the $\pi\lambda \times \pi\lambda$ TG cells. Throughout this section, we use $\lambda = 2$ nm so that the JP phases occupy about nine cells.

In both cases, $\dot{\gamma}$ is the shear rate. The flow rate $\lambda\dot{\gamma}$ is chosen so that (24) has the same rate of viscous dissipation per area as for (23). In other words, $\int_A \frac{1}{2}\mu|\nabla\mathbf{u} + \nabla\mathbf{u}^T|^2 dA$ is the same for $\mathbf{u} = \mathbf{u}_\infty^{\text{sh}}$ as for $\mathbf{u} = \mathbf{u}_\infty^{\text{TG}}$ when integrated over a TG cell A .

To obtain a range for $\dot{\gamma}$, consider the capillary number

$$\text{Ca} = \frac{\mu\dot{\gamma}R^3}{\kappa}, \quad (25)$$

where $R = 10$ nm and $\kappa = 20 k_B T$ are the characteristic phase-sample radius and bending rigidity, respectively. That is, κ gives the elastic stress for restoring the phase-sample shape. Shear stress overcomes elastic stress when $\text{Ca} > 1$, and this yields $\dot{\gamma} > 2 \times 10^{-2} \text{ ns}^{-1} = 2 \times 10^6 \text{ s}^{-1}$. Thus our values for $\dot{\gamma}$ range between 0 ns^{-1} , corresponding to quiescent flow, and 0.2 ns^{-1} , capable of rupturing the sample. Such shear rates are compatible with molecular dynamics simulations [27], those for large unilamellar vesicles (LUVs), [51], and shearing in blood capillary vessels [52] where shear rates range over 100 – 2000 s^{-1} . From the particle diffusion time D/L^2 and advection time $L/u = (\dot{\gamma})^{-1}$, $D = 0.17 \times 10^{-9} \text{ m}^2 \text{ s}^{-1}$ and $L \sim 10$ nm, we obtain a Péclet number $\text{Pe} = (D/L^2)/(L/u) \sim 60$, suggesting that advection dominates the particle transport.

For initial data, note that the steady-state type I amphiphiles phase consists of a number of disjoint bilayer components [Fig. 2(b)]. To also have a single-component type I phase, we reinitialize the data to have a ring-shaped vesicle bilayer. This phase is distinguished from “bilayer” by “vesicle BL” in the figures. For the same number of JPs, the vesicle bilayer has lower free steady-state energy ($F = 24.6 k_B T \text{ nm}^{-1}$) than the disordered bilayer phase ($F = 27.2 k_B T \text{ nm}^{-1}$). Since the simulations are for two dimensions, multiplying F by a length gives the energy of a transversely invariant, three-dimensional phase.

The simulation setup consists of placing each of the phases in either a shear or TG background flow and then solving for the particle trajectories in time. In each setup, we solve for 500 time steps with $\Delta t = 2$ ns, yielding time courses for $t \in [0, T]$, $T = 1 \mu\text{s}$. We then postprocess the trajectories.

Figures 3(e)–3(l) show the typical streamlines for JP phases in background flow. Although the plots only show the region near the JPs, the fluid velocity \mathbf{u} and order parameter u are accounted for in all of \mathbb{R}^2 . Moreover, \mathbf{u} satisfies the rigid boundary condition at every JP-fluid interface, i.e., the particles interact with the local flow field and are not merely carried by background flow. See Sec. S1 of the Supplemental Material for movies showing the dynamics of the JP suspensions in Fig. 3 [49].

Figures S1–S8 in the Supplemental Material contain the fully resolved time courses for the free energy F , alignment order S_2 , and strain E [49]. The eight setups correspond to the four JP phases—bilayer, vesicle BL, multilamellar, and striated—and two background flows—shear and TG. The data are plotted with the same vertical and horizontal axes to facilitate comparisons between simulation setups. Each setup considers a range of shear rates $\dot{\gamma}$ in the interval $[0, 0.2] \text{ ns}^{-1}$.

The fully resolved time courses in Figs. S1–S8 in the Supplemental Material contain significant oscillations due to the particle-based formulation and tumbling inherent to the background flows [49]. To extract meaningful data, we further postprocess the F , S_2 , and E curves by taking their time average over the interval $t \in [0, T]$.

A. Strain and alignment

The plots reveal highly distinct material responses from each phase. Figures 3(a) and 3(b) show the time-averaged strain $\frac{1}{T} \int_0^T E dt$ over a broad range of shear rates. Strain E measures the non-rigid-body deformation relative to the initial state and expectedly increases with shear rate. The greatest increase occurs with the type I amphiphiles, suggesting that this phase has the lowest elastic

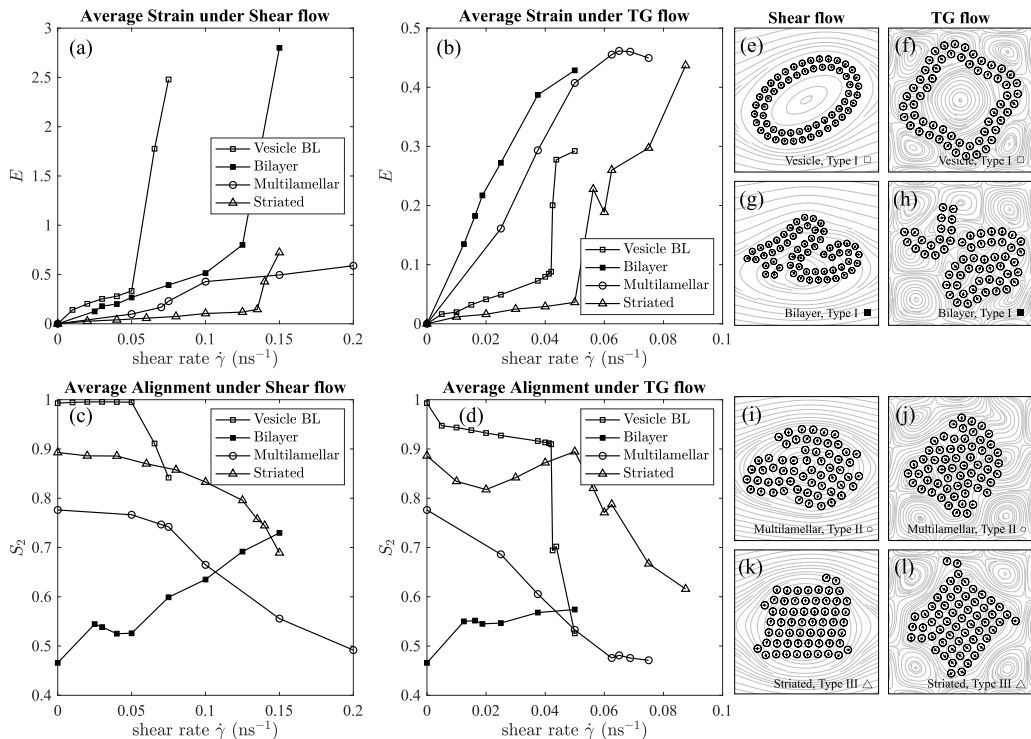


FIG. 3. (a) and (b) show the average strain increase for bilayer, vesicle BL, multilamellar, and striated JP structures under a shear flow and a TG flow, respectively. (c) and (d) show the average alignment of the four JP structures under a shear flow and a TG flow, respectively. Each snapshot in (e)–(l) contains the configuration of the JP structure without ruptures using a specific type of boundary condition, and the background curves indicate the velocity streamlines.

modulus (squares). In comparison, the striated phase consisting of type III polar JP is basically rigid (triangles).

Figures 3(c) and 3(d) plot the time-averaged alignment order S_2 . The vesicle and striated phases possess the greatest alignment order, and for the most part, S_2 decreases with increases in shear rate. However, there is an exception. The type I bilayer phase alignment order actually increases under both shear and TG flows (solid squares). This suggests that the mixing action of background flow has the effect of moving the disordered bilayer phase out of a local equilibrium and into a state with greater order. This surprising increase, brought about by combining previously broken bilayer end caps, is accompanied by a slight decrease in free energy [Fig. 4(a), solid squares].

The sudden jumps in Figs. 3(a) and 3(b) and commensurate drops in Figs. 3(c) and 3(d) indicate the existence of a critical shear rate $\dot{\gamma}_*$. This means that for $\dot{\gamma} < \dot{\gamma}_*$, the JP phase remains intact while for $\dot{\gamma} > \dot{\gamma}_*$, the phase ruptures. For example, the vesicle BL phase has $\dot{\gamma}_*$ of approximately 0.05 ns⁻¹ under shear flow and TG flow. However, the critical shear rate is flow pattern dependent because the striated phase has $\dot{\gamma}_* = 0.14$ ns⁻¹ under shear flow while $\dot{\gamma}_* = 0.05$ ns⁻¹ under TG flow. Due to variable stress distribution, the critical shear rate in TG flow likely depends on the cell size parameter λ . The disordered bilayer phase does not really possess a critical shear rate because it already consists of several, disjoint components. The jump in Fig. 3(a) (solid squares) simply corresponds to disjoint components drifting apart in the shear flow. The type II multilamellar phase did not rupture for any of the shear rates considered.

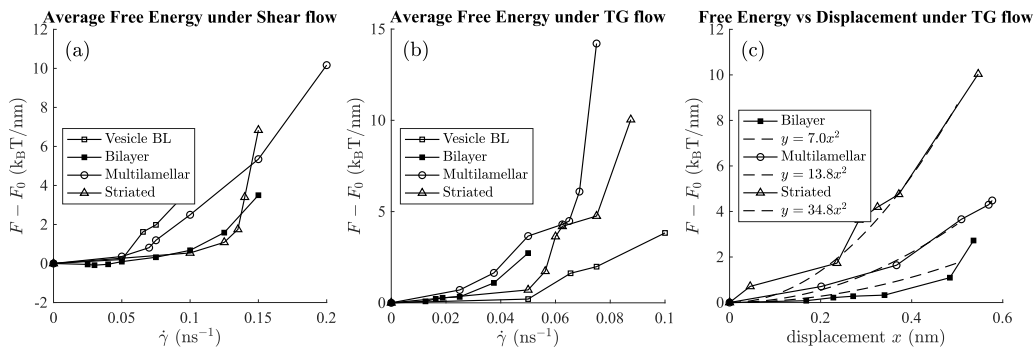


FIG. 4. The change in average free energy vs shear rates for shear flow and TG flow simulation results is plotted in (a) and (b). (c) contains quadratic fits to the change in free energy as a function of displacement in interparticle distance from equilibrium.

B. Free energy

Figure 4 plots the time-averaged relative free energy $\frac{1}{T} \int_0^T (F - F_0) dt$, where F_0 is (19) at $t = 0$. The greatest increase occurs with the type II multilamellar phase, with the other phases showing a moderate change in a few $k_B T \text{ nm}^{-1}$.

Figure 4(c) plots the free energy against the displacement $x = cE$ representing the change in mean interparticle displacement from equilibrium; $c = 1.25 \text{ nm}$ is the particle radius. The energies in Fig. 4(c) are essentially quadratic in x suggesting that the interactions are harmonic locally around equilibrium. The harmonic bond strength is strongest between polar JPs, and it is greater by factors of 2 and 5 than that for asymmetric hydrophobes and amphiphiles, respectively. This makes sense when considering that the free energy of the steady-state striated phase is also greatest [Fig. 2(c), around $85 k_B T \text{ nm}^{-1}$]. However, the bond strength in the multilamellar phase comes in second, despite having the least steady-state free energy (around $15 k_B T \text{ nm}^{-1}$). The data point to the fact that the binding properties do not only scale with free energy, but also involve the details of the interface's hydrophobicity, which are tuned by (18) in our model.

C. Rheology

So far, we have considered static material properties, namely, constant strains maintained by an external force provided by background flow. Now we consider dynamic material properties. Specifically, we look at the strain rate

$$\dot{E} = \left(\frac{1}{T} \int_0^T \left| \frac{dE}{dt} \right|^2 dt \right)^{1/2}. \quad (26)$$

The reason for defining \dot{E} in this way is that the shear flow $\mathbf{u}_\infty^{\text{sh}}$ simulations correspond to a complex fluid within a drag plate rheometer where the shear stress is set by $\mu \dot{\gamma}$ and the observed, sample shear rate is \dot{E} . The definitions carry over to the TG flow case directly. Also, as a practical consideration, the rotation of nonisotropic JP phases in the background flow leads to oscillation in the strain time courses making systematic fitting challenging (see Supplemental Material, Figs. S1–S8 [49]). The integral in (26) averages out these oscillations and gives physically meaningful values.

The shear stress-strain rate data are excellently fit by power laws. Figures 5(a)–5(c) show the data for type I, type II, and type III JPs, respectively, under both shear flow (squares) and TG flow (triangles). The bilayer phases consisting of type I JPs are basically Newtonian with viscosity $0.014 \text{ MPa } \mu\text{s} = 14 \text{ mPa s}$, about 14 times the viscosity of water at room temperature [Fig. 5(a), dashed curve]. The vesicle bilayer phase is slightly shear thickening [Fig. 5(a), solid curve]. Similar

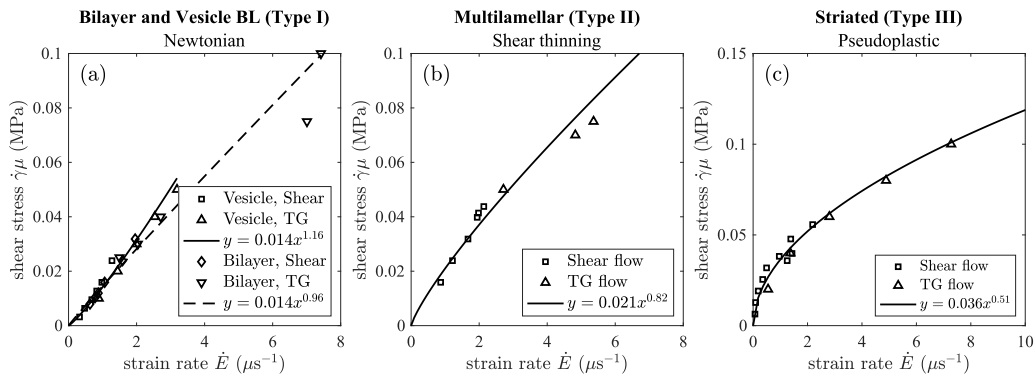


FIG. 5. Rheology of type I, II, and III phases. (a) shows that bilayer phases behave as a Newtonian fluid. (b) provides that the multilamellar phase shows a near-shear-thinning behavior. A pseudoplastic behavior of deformation in striated phases is shown in (c).

shear thickening behaviors are found in continuum vesicle models [53,54]. The multilamellar phase consisting of type II JPs is somewhat shear thinning, but its viscosity is larger than for type I. Finally, the striated phase is strongly shear thinning. This further explains the rigidlike behavior of the striated phase found in the strain, shear-rate relationships from Figs. 3(a) and 3(b) (triangles).

D. Discussion

We choose the range of shear rates $\dot{\gamma} \in [0, 0.02] \text{ ns}^{-1}$ by analyzing the capillary number of the JP phases. With this range, there is a critical shear rate $\dot{\gamma}_*$ for the vesicle BL and striated phases where shear stresses exceeded elastic stresses, leading to rupture. The multilamellar phase did not rupture. By varying model parameters, we perform a dimensional analysis on $\dot{\gamma}_*$. Focusing on type III JPs in shear flow, $\dot{\gamma}_* = 0.14 \text{ ns}^{-1}$ for the basic model parameters (see Sec. III). Increasing and decreasing the tension parameters γ and M by up to 10% (collectively denoted $\Delta\gamma/\gamma$) led to basically the same relative increase or decrease in critical shear rate (denoted $\Delta\dot{\gamma}_*/\dot{\gamma}_*$). This suggests that the critical shear rate scales linearly with the tension parameters. Conversely, increasing (decreasing) the length parameters c (particle radius), ρ , and ρ_0 by up to 10% (collectively denoted $\Delta c/c$) leads to roughly twice the relative decrease (increase) in the critical shear rate. This points to an inverse-quadratic scaling in length. Figure 6(a) summarizes the findings and suggests the scaling

$$\mu\dot{\gamma}_* = K_{\text{III}} \frac{\gamma L}{c^2}. \quad (27)$$

The scalar K_{III} is specific to the striated phase under shear flow. Here, L is the diameter of the phase sample, which is proportional to γ^* since the striated phase tends to cleave during rupture (see movie in the Supplemental [49]). Our previous work [19] found the scaling $\mu\dot{\gamma}_* = K_1\gamma c^2/(\rho L^2)$ for a vesicle BL in shear flow.

So far, Sec. V has shown that variations in free energy and strain generally depend on the distribution of fluid stresses, i.e., shear versus TG flow. To further illustrate how fluid stresses interact with the geometry of the JP phases, we initialize a circular vesicle bilayer in various TG-flow cell sizes λ ranging from $\lambda = 1 \text{ nm}$ in Fig. 6(b) to $\lambda = 4 \text{ nm}$ in Fig. 6(e). These JP vesicles fluctuate and deform around the steady shape of an octagon ($\lambda = 1 \text{ nm}$), a dimpled square ($\lambda = 2 \text{ nm}$), a rounded diamond ($\lambda = 3 \text{ nm}$), and a rounded rectangle ($\lambda = 4 \text{ nm}$). See Sec. S1 of the Supplemental Material for a movie showing the dynamics of the JP vesicle for the four different values of λ in Figs. 6(b)–6(e) [49].

For $\lambda = 1 \text{ nm}$ and $\lambda = 2 \text{ nm}$, multiple TG cells are inside the JP vesicle as the inner leaflet of JPs moves clockwise along the boundary faster than the outer leaflet. For $\lambda = 3 \text{ nm}$ and $\lambda = 4$

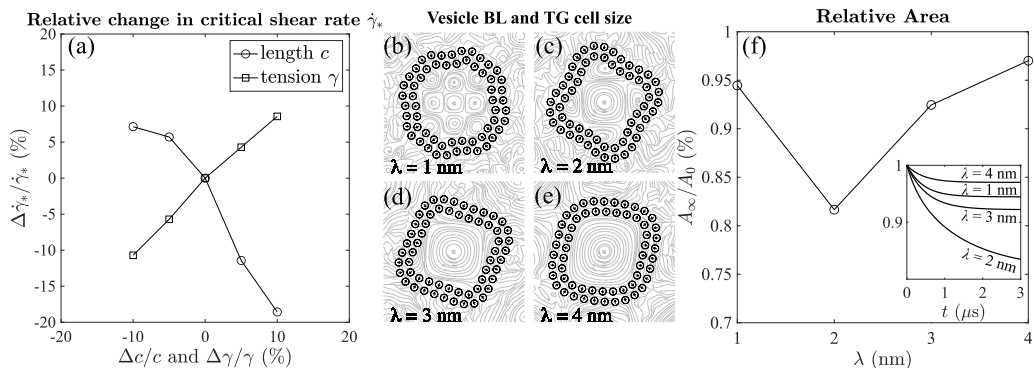


FIG. 6. In (a), the relative change in $\dot{\gamma}_*$ is linear in the relative change of the tension parameters γ and M with slope 1. Additionally, the relative change in $\dot{\gamma}_*$ has slope -2 with respect to the relative change in the length parameters c , ρ , and ρ_0 . (b)–(e) show the tank-treading configurations of a vesicle bilayer; the configurations with streamlines of a vesicle are for a TG flow at $t = 1 \mu\text{s}$ with $\lambda = 1, 2, 3, 4$, respectively. In (f), inset, the relative enclosed area A/A_0 for the four cases in (b)–(e) decays to a steady state. The steady-state A_∞/A_0 relative area is nonmonotonic in λ .

nm, there is only one TG cell inside the JP vesicle, and the JPs in the bilayer tank-tread in the counterclockwise direction [Figs. 6(b)–6(e)]. Finally, we calculated the vesicle area A and length L . As shown in Fig. 6(f), the relative area achieves a steady state A_∞/A_0 that is greatest for $\lambda = 4$ nm yet least for $\lambda = 2$ nm. The relative length L/L_0 , however, is constant in t for all cell sizes (data not shown). In other words, the fluid-structure interactions of JPs give rise to nonmonotonic dependence of membrane permeability on the TG cell size λ . Such dynamic permeability due to fluid-structure interactions is also found in the clogging of spherical particles in a rectangular microfluidic channel [55].

We have excluded thermal fluctuations because they are unresolved in the JP phases we consider. For a tensionless, planar membrane, the Fourier coefficients for the profile height $h(\mathbf{x}) = \sum_{\mathbf{k}} h(\mathbf{k})e^{i\mathbf{k}\cdot\mathbf{x}}$ satisfy [56]

$$\langle |h(\mathbf{k})|^2 \rangle = \frac{k_B T}{L_x L_y \kappa} \frac{1}{|\mathbf{k}|^4}, \quad (28)$$

where \mathbf{x} is a point in an $L_x \times L_y$ rectangular membrane patch, $\mathbf{k} = (2\pi m/L_x, 2\pi n/L_y)$ with $m, n \in \mathbb{Z}$, not both zero, and κ is the membrane bending modulus.

To estimate $h(\mathbf{k})$, the $N_b = 60$ JP vesicle in Fig. 3(e) has arclength $L_x \approx 50$ nm. Our prior work [18,19] gave $\kappa \approx 20 k_B T$. Since our simulations are two dimensional, we restrict our attention to transversely invariant fluctuations where $n = 0$. Substituting these values gives

$$\langle |h(\mathbf{k})|^2 \rangle \approx \frac{4 \text{ nm}^3}{L_y} \frac{1}{m^4}, \quad m = \pm 1, \pm 2, \dots \quad (29)$$

For any moderate transverse depth, say, $L_y > 4$ nm, the leading Fourier coefficient has a magnitude less than 1 nm with the remaining coefficients dropping off to zero precipitously. The expected amplitudes coming from thermal fluctuations are therefore negligible compared with particle size. The elastic moduli for the type II and type III phases are greater by a factor of 2 and 5, respectively, than those for type I [Fig. 4(c)], making thermal fluctuation even more negligible in these cases.

The fact that the fluctuation amplitudes are small is not a consequence of stiffness. Quite the opposite, the value $\kappa = 20 k_B T$ agrees with the experimental literature where micrometer-sized vesicles observably fluctuate [57]. Rather, because the wave vector \mathbf{k} is inversely proportional to the characteristic size of L_x and L_y , larger energies are required to fluctuate membranes over

smaller wavelengths, and these energies exceed the available thermal energy when the wavelengths approach tens of nanometers as demonstrated above.

The calculated viscosities—14 mPa s for type I JP phases and 21 mPa s for type II JP phases—are physically reasonable. In two-dimensional dilute suspensions, the Einstein viscosity correction is $1 + 2\phi + 4\phi^2 + O(\phi^3)$, where $\phi \ll 1$ is the volume fraction [58–61]. In Figs. 3(e)–3(h), the volume fraction is $\phi \approx 0.5$, which would correspond to an effective shear viscosity of 4 mPa s according to Einstein’s viscosity correction. Note, however, that since $\phi = 0.5$ is outside of the dilute limit, one expects viscosities ten or more times greater than the viscosity of water [62], and a number of analytical and numerical approaches have been successfully applied to these dense suspensions [63].

Further parametric studies are required to differentiate between passive effects and JPs’ preferred alignments. For example, the difference between the values 14 mPa s for type I JPs and 21 mPa s for type II JPs can be explained by the fact that the multilamellar phase is more tightly packed than the bilayer phase [Figs. 3(e)–3(h)]. Furthermore, it seems that the viscosity, and the tendency toward shear thinning in the case of type III JPs where viscosity is effectively infinite for low strain rates [Fig. 5(c)], is related to particle coordination. That is, a single JP coordinates with the following: one neighbor in the apposing bilayer for type I, two neighbors at the tail and head interfaces for type II, and four neighbors (front, back, left, and right) for type III.

Scaling laws for the “virial viscosity,” the nonhydrodynamic part of the relative viscosity in steady shear, have been determined experimentally [64]. Other simulation studies have investigated the rheology of strain-hardening capsules as a function of membrane inextensibility using the three-dimensional immersed boundary method [65], studied dilute suspensions of compound particles [66], and shown how shear thickening in systems with widely different particle properties arises when adhesion forces bring particles into frictional contact [67]. Within this context, membrane inextensibility in the case of type I amphiphiles and adhesion in general can be inferred from the functional relationships between free energy and displacement in Fig. 4(c), for example.

For active particles, researchers have obtained analytical expressions for the effective viscosity resulting from the activity of dilute swimmers in extensional flows [68] and compared numerical predictions under shear flow derived from Stokesian dynamics and lubrication theory [69]. Suspensions of pushers can yield an apparent reduction in viscous dissipation arising from particle activity. In contrast, the JP suspensions of the present study do not inject, but rather store energy coming from the background flow.

VI. CONCLUSION

In this paper, we employ the newly developed JP model using BIEs [18,19] and tune the boundary conditions with energy normalization to study the collective dynamics of amphiphilic (type I), biased hydrophobic (type II), and bipolar (type III) JPs under various flowing conditions (quiescent flow, linear shear flow, and Taylor-Green flow). Three quantities are computed to characterize the dynamics of the collective configurations of JPs: the free energy F , the strain parameter E , and the scalar order parameter S_2 . Under a given flow, we use these three measures of deformations to quantify the differences in the collective dynamics between the three types of JPs. These results, summarized below, provide general insight into the dynamic control of active particles in a viscous suspension.

In a quiescent flow, the free-energy profiles demonstrate that the relaxation process for particles confined in a certain size of box is independent of the number of particles. However, we find that the final configuration does depend on the initial distribution of particle directors \mathbf{d}_i . Therefore multiple patterns or local energy minimum states may appear depending on the initial setup.

Under a relatively weak linear shear flow, the amphiphilic JPs behave as a unilamellar vesicle that elongates and tank-treads, with the scalar order parameter increasing over time. The assembly of multilamellar and striated JP structures resembles a rigid body motion with minimal deformation. The effective viscosity of the material quantitatively validates this result. High-shear-rate cases

provide a range of critical shear rates where the structures break apart and undergo topological changes. We further show that free energy, scalar order parameter, and strain are effective measures to quantitatively capture the collective hydrodynamics of JPs under a linear shear flow.

Under a Taylor-Green flow, the amphiphilic JPs are the most interesting, exhibiting different vesicle shapes depending on the ratio of the size of the TG flow to the vesicle size. These results show that the shape of the vesicle, whether square or polygonal, can be controlled by adjusting the size of the cell in the TG flow. In addition, the permeability of the JP bilayer varies nonmonotonically with the TG cell size. On the other hand, the assembly of multilamellar JPs and the striated JPs behave more like a rigid body with connected subdomains, and the number of subdomains increases with increasing strength of the TG flow. Overall, the multilamellar (type II) JP assembly behaves as a shear thinning fluid, while the striated (type III) JP assembly possesses a yield stress.

The results reported here make inroads into a modeling framework for hydrodynamics of active colloids [3,14,70,71]. The present study also helps us to understand the rheology of JP oligomers that may be realized in experiments. We are extending this study to three-dimensional systems with more realistic features such as size distributions of JPs and thermal fluctuations [36]. From a numerical perspective, it is straightforward to include random perturbations in the particle shape and boundary condition that mimic interfacial properties found under laboratory conditions [4,10,11,17].

ACKNOWLEDGMENTS

We thank the anonymous referees for pointing out the Péclet number, capillary number, and fluctuation analysis. E. Corona, M. Rachh, S. Jiang, and T. Beck provided useful insights. B.Q. acknowledges support from the Simons Foundation, Mathematics and Physical Sciences Division, Collaboration Grants for Mathematicians, Award No. 527139. Y.-N.Y. acknowledges support from the NSF (Grants No. DMS 1614863 and No. DMS 195160) and the Flatiron Institute.

APPENDIX

The boundary integral calculation of (19) relies on the following identity:

$$\nabla u(\mathbf{x}) \cdot \mathbf{v}_x = -\frac{1}{\rho^2} \mathbf{t}_x \cdot S[\sigma \mathbf{t}](\mathbf{x}) + \frac{d}{ds} S\left[\frac{d\sigma}{ds}\right](\mathbf{x}), \quad \mathbf{x} \in \partial\Omega. \quad (\text{A1})$$

Here, \mathbf{t}_x is the tangent vector and d/ds is the arclength derivative. Substituting (A1) into (19) for the normal derivative leads to the single layer, S , which is more straightforward to evaluate. The arclength derivative is computed using the spectrally accurate Fourier differentiation.

To prove (A1), let

$$S[\sigma](\mathbf{x}) = \int_{\partial\Omega} G(\mathbf{x} - \mathbf{y}) \sigma(\mathbf{y}) ds_y \quad (\text{A2})$$

be the single-layer potential for a density function σ . Fix $\mathbf{x} \in \partial\Omega$, let \mathbf{v}_x and \mathbf{v}_y be the unit normal at \mathbf{x} and \mathbf{y} , respectively, in $\partial\Omega$, and let $\mathbf{z} \in \Omega$. The subscripts in ∇_z and ∇_y denote differentiation with respect to \mathbf{z} and \mathbf{y} , respectively.

Recall from (11) that $u = \mathcal{D}[\sigma]$. Then

$$\begin{aligned} \nabla_z u(\mathbf{z}) \cdot \mathbf{v}_x &= \mathbf{v}_x \cdot \nabla_z \int_{\partial\Omega} \frac{\partial G(\mathbf{z} - \mathbf{y})}{\partial \mathbf{v}_y} \sigma(\mathbf{y}) ds_y \\ &= \int_{\partial\Omega} \mathbf{v}_x^\top (\nabla_z \nabla_y^\top G(\mathbf{z} - \mathbf{y})) \mathbf{v}_y \sigma(\mathbf{y}) ds_y \\ &= - \int_{\partial\Omega} \mathbf{v}_x^\top (\nabla_y \nabla_y^\top G(\mathbf{z} - \mathbf{y})) \mathbf{v}_y \sigma(\mathbf{y}) ds_y, \end{aligned}$$

since we can interchange $\nabla_{\mathbf{z}}$ with $-\nabla_{\mathbf{y}}$. Following the work of Hsiao and Wendland [37] (see Sec. 1.2 therein),

$$\mathbf{v}_{\mathbf{x}}^{\top}(\nabla_{\mathbf{y}}\nabla_{\mathbf{y}}^{\top}G(\mathbf{z}-\mathbf{y}))\mathbf{v}_{\mathbf{y}} = -\mathbf{t}_{\mathbf{x}}^{\top}(\nabla_{\mathbf{y}}\nabla_{\mathbf{y}}^{\top}G(\mathbf{z}-\mathbf{y}))\mathbf{t}_{\mathbf{y}} + \Delta_{\mathbf{y}}G(\mathbf{z}-\mathbf{y})\mathbf{t}_{\mathbf{x}} \cdot \mathbf{t}_{\mathbf{y}}. \quad (\text{A3})$$

Then, using that $\Delta_{\mathbf{y}}G(\mathbf{z}-\mathbf{y}) = \rho^{-2}G(\mathbf{z}-\mathbf{y})$, interchanging $\nabla_{\mathbf{y}}$ with $-\nabla_{\mathbf{z}}$ once more, and integrating by parts in arclength s , we obtain

$$\begin{aligned} \nabla_{\mathbf{z}}u(\mathbf{z}) \cdot \mathbf{v}_{\mathbf{x}} &= - \int_{\partial\Omega} \Delta_{\mathbf{y}}G(\mathbf{z}-\mathbf{y})\mathbf{t}_{\mathbf{x}} \cdot \mathbf{t}_{\mathbf{y}}\sigma(\mathbf{y}) ds_{\mathbf{y}} + \int_{\partial\Omega} (\mathbf{t}_{\mathbf{x}} \cdot \nabla_{\mathbf{y}})(\mathbf{t}_{\mathbf{y}} \cdot \nabla_{\mathbf{y}}G(\mathbf{z}-\mathbf{y}))\sigma(\mathbf{y}) ds_{\mathbf{y}} \\ &= - \int_{\partial\Omega} \frac{1}{\rho^2}G(\mathbf{z}-\mathbf{y})\mathbf{t}_{\mathbf{x}} \cdot \mathbf{t}_{\mathbf{y}}\sigma(\mathbf{y}) ds_{\mathbf{y}} - (\mathbf{t}_{\mathbf{x}} \cdot \nabla_{\mathbf{z}}) \int_{\partial\Omega} \frac{d}{ds_{\mathbf{y}}}G(\mathbf{z}-\mathbf{y})\sigma(\mathbf{y}) ds_{\mathbf{y}} \\ &= - \frac{1}{\rho^2}\mathbf{t}_{\mathbf{x}} \cdot \int_{\partial\Omega} G(\mathbf{z}-\mathbf{y})\mathbf{t}_{\mathbf{y}}\sigma(\mathbf{y}) ds_{\mathbf{y}} + (\mathbf{t}_{\mathbf{x}} \cdot \nabla_{\mathbf{z}}) \int_{\partial\Omega} G(\mathbf{z}-\mathbf{y})\frac{d}{ds}\sigma(\mathbf{y})ds_{\mathbf{y}}. \end{aligned}$$

Letting $\mathbf{z} \rightarrow \mathbf{x} \in \partial\Omega$, and noting that both sides of the equation are continuous, we obtain (A1).

-
- [1] P. G. de Gennes, Soft matter, *Rev. Mod. Phys.* **64**, 645 (1992).
- [2] A. Kirillova, C. Marschelke, and A. Synytska, Hybrid Janus particles: Challenges and opportunities for the design of active functional interfaces and surfaces, *ACS Appl. Mater. Interfaces* **11**, 9643 (2019).
- [3] C. H. Meredith, A. C. Castonguay, Y.-J. Chiu, A. M. Brooks, P. G. Moerman, P. Torab, P. K. Wong, A. Sen, D. Velegol, and L. D. Zarzar, Chemical design of self-propelled Janus droplets, *Matter* **5**, 616 (2022).
- [4] L. C. Bradley, W.-H. Chen, K. J. Stebe, and D. Lee, Janus and patchy colloids at fluid interfaces, *Curr. Opin. Colloid Interface Sci.* **30**, 25 (2017).
- [5] C. Kang and A. Honciuc, Self-assembly of Janus nanoparticles into transformable suprastructures, *J. Phys. Chem. Lett.* **9**, 1415 (2018).
- [6] L. Hong, A. Cacciuto, E. Luijten, and S. Granick, Clusters of amphiphilic colloidal spheres, *Langmuir* **24**, 621 (2008).
- [7] F. Gheisari, M. Shafiee, M. Abbasi, A. Jangjou, P. Izadpanah, A. Vaez, and A. M. Amani, Janus nanoparticles: an efficient intelligent modern nanostructure for eradicating cancer, *Drug Metab. Rev.* **53**, 592 (2021).
- [8] Y. Liu, X. Yang, Z. Huang, P. Huang, Y. Zhang, L. Deng, Z. Wang, Z. Zhou, Y. Liu, H. Kalish, N. M. Khachab, X. Chen, and Z. Nie, Magneto-plasmonic Janus vesicles for magnetic field-enhanced photoacoustic and magnetic resonance imaging of tumors, *Angew. Chem., Int. Ed.* **55**, 15297 (2016).
- [9] J. Li, J. Wang, Q. Yao, K. Yu, Y. Yan, and J. Zhang, Cooperative assembly of Janus particles and amphiphilic oligomers: The role of Janus balance, *Nanoscale* **11**, 7221 (2019).
- [10] L. C. Bradley, K. J. Stebe, and D. Lee, Clickable Janus particles, *J. Am. Chem. Soc.* **138**, 11437 (2016).
- [11] L. D. Zarzar, V. Sresht, E. M. Sletten, J. A. Kalow, D. Blankschtein, and T. M. Swager, Dynamically reconfigurable complex emulsions via tunable interfacial tensions, *Nature (London)* **518**, 520 (2015).
- [12] M. F. Hagan and G. M. Grason, Equilibrium mechanisms of self-limiting assembly, *Rev. Mod. Phys.* **93**, 025008 (2021).
- [13] Y. Collard, G. Grosjean, and N. Vandewalle, Magnetically powered metachronal waves induce locomotion in self-assemblies, *Commun. Phys.* **3**, 112 (2020).
- [14] H. R. Vutukuri, M. Hoore, C. Abaurrea-Velasco, L. van Buren, A. Dutto, T. Auth, D. A. Fedosov, G. Gompper, and J. Vermant, Active particles induce large shape deformations in giant lipid vesicles, *Nature (London)* **586**, 52 (2020).
- [15] F. Boccardo and O. Pierre-Louis, Controlling the Shape of Small Clusters with and without Macroscopic Fields, *Phys. Rev. Lett.* **128**, 256102 (2022).
- [16] V. N. Manoharan, Colloidal matter: Packing, geometry, and entropy, *Science* **349**, 1253751 (2015).

- [17] A. Kirillova, G. Stoychev, L. Ionov, and A. Synytska, Self-assembly behavior of hairy colloidal particles with different architectures: Mixed versus Janus, *Langmuir* **30**, 12765 (2014).
- [18] S.-P. P. Fu, R. Ryham, A. Klöckner, M. Wala, S. Jiang, and Y.-N. Young, Simulation of multiscale hydrophobic lipid dynamics via efficient integral equation methods, *Multiscale Model. Simul.* **18**, 79 (2020).
- [19] S.-P. Fu, B. Quaife, R. Ryham, and Y.-N. Young, Two-dimensional vesicle hydrodynamics from hydrophobic attraction potential, *J. Fluid Mech.* **941**, A41 (2022).
- [20] J. F. Nagle and S. Tristram-Nagle, Structure of lipid bilayers, *Biochim. Biophys. Acta Rev. Biomembr.* **1469**, 159 (2000).
- [21] T. Krüger, S. Frijters, F. Günther, B. Kaoui, and J. Harting, Numerical simulations of complex fluid-fluid interface dynamics, *Eur. Phys. J.: Spec. Top.* **222**, 177 (2013).
- [22] N. Grandmaison, D. Brancherie, and A.-V. Salsac, Modelling of damage of a liquid-core microcapsule in simple shear flow until rupture, *J. Fluid Mech.* **914**, A25 (2021).
- [23] M. Er-Rafik, K. Ferji, J. Combet, O. Sandre, S. Lecommandoux, M. Schmutz, J.-F. Le Meins, and C. M. Marques, Tear of lipid membranes by nanoparticles, *Soft Matter* **18**, 3318 (2022).
- [24] S. R. Keller and R. Skalak, Motion of a tank-treading ellipsoidal particle in a shear flow, *J. Fluid Mech.* **120**, 27 (1982).
- [25] R. Finken, A. Lamura, U. Seifert, and G. Gompper, Two-dimensional fluctuating vesicles in linear shear flow, *Eur. Phys. J. E* **25**, 309 (2008).
- [26] H. Zhao and E. S. G. Shaqfeh, The dynamics of a vesicle in simple shear flow, *J. Fluid Mech.* **674**, 578 (2011).
- [27] A. F. Brandner, S. Timr, S. Melchionna, P. Derreumaux, M. Baaden, and F. Sterpone, Modelling lipid systems in fluid with lattice Boltzmann molecular dynamics simulations and hydrodynamics, *Sci. Rep.* **9**, 16450 (2019).
- [28] M. Banik, S. Sett, C. Bakli, A. K. Raychaudhuri, S. Chakraborty, and R. Mukherjee, Substrate wettability guided oriented self assembly of Janus particles, *Sci. Rep.* **11**, 1182(2021).
- [29] F.-F. Hu, Y.-W. Sun, Y.-L. Zhu, Y.-N. Huang, Z.-W. Li, and Z.-Y. Sun, Enthalpy-driven self-assembly of amphiphilic Janus dendrimers into onion-like vesicles: a Janus particle model, *Nanoscale* **11**, 17350 (2019).
- [30] S. Marčelja, Structural contribution to solute-solute interaction, *Croat. Chem. Acta* **49**, 347 (1977).
- [31] G. Gompper, M. Hauser, and A. A. Kornyshev, “Confined” water and hydrophobic attraction as a result of metastable coordination, stabilized by hydrophobic surfaces, *J. Chem. Phys.* **101**, 3378 (1994).
- [32] J. C. Eriksson, S. Ljunggren, and P. M. Claesson, A phenomenological theory of long-range hydrophobic attraction forces based on a square-gradient variational approach, *J. Chem. Soc., Faraday Trans. 2* **85**, 163 (1989).
- [33] Q. Lin, E. E. Meyer, M. Tadmor, J. N. Israelachvili, and T. L. Kuhl, Measurement of the long- and short-range hydrophobic attraction between surfactant-coated surfaces, *Langmuir* **21**, 251 (2005).
- [34] J. N. Israelachvili, S. Marčelja, and R. G. Horn, Physical principles of membrane organization, *Q. Rev. Biophys.* **13**, 121 (1980).
- [35] Q. Hang and Q. Wang, A hybrid phase field method for fluid-structure interactions in viscous fluids, [arXiv:2109.07361](https://arxiv.org/abs/2109.07361).
- [36] R. Kohl, E. Corona, V. Cheruvu, and S. Veerapaneni, Fast and accurate solvers for simulating Janus particle suspensions in Stokes flow, [arXiv:2104.14068](https://arxiv.org/abs/2104.14068).
- [37] G. C. Hsiao and W. L. Wendland, *Boundary Integral Equations* (Springer, Berlin, 2008).
- [38] H. Power and G. Miranda, Second kind integral equation formulation of Stokes’ flows past a particle of arbitrary shape, *SIAM J. Appl. Math.* **47**, 689 (1987).
- [39] C. Pozrikidis, *Boundary Integral and Singularity Methods for Linearized Viscous Flow* (Cambridge University Press, New York, 1992).
- [40] M. Rachh and L. Greengard, Integral equation methods for elastance and mobility problems in two dimensions, *SIAM J. Numer. Anal.* **54**, 2889 (2016).
- [41] E. Corona, L. Greengard, M. Rachh, and S. Veerapaneni, An integral equation formulation for rigid bodies in Stokes flow in three dimensions, *J. Comput. Phys.* **332**, 504 (2017).

- [42] B. Quaife and G. Biroso, High-volume fraction simulations of two-dimensional vesicle suspensions, *J. Comput. Phys.* **274**, 245 (2014).
- [43] D. Boal, *Mechanics of the Cell*, 2nd ed. (Cambridge University Press, Cambridge, 2012).
- [44] P. I. Kuzmin, S. A. Akimov, Y. A. Chizmadzhev, J. Zimmerberg, and F. S. Cohen, Line tension and interaction energies of membrane rafts calculated from lipid splay and tilt, *Biophys. J.* **88**, 1120 (2005).
- [45] A. D. Petelska, Interfacial tension of bilayer lipid membranes, *Cent. Eur. J. Chem.* **10**, 16 (2012).
- [46] M. B. Jackson, The hydrophobic effect in solute partitioning and interfacial tension, *Sci. Rep.* **6**, 19265(2016).
- [47] A. J. García-Sáez, S. Chiantia, and P. Schwille, Effect of line tension on the lateral organization of lipid membranes, *J. Biol. Chem.* **282**, 33537 (2007).
- [48] S. Marčelja and N. Radic, Repulsion of interfaces due to boundary water, *Chem. Phys. Lett.* **42**, 129 (1976).
- [49] See Supplemental Material at <http://link.aps.org/supplemental/10.1103/PhysRevFluids.8.050501> for movies showing the transitions from initial, randomized configurations to final, steady-state configurations; movies showing JP phases under background flows; and the fully resolved simulation time courses organized in terms of the bilayer, vesicle BL, multilamellar, and striated JP configurations under shear flow and under TG flow.
- [50] J. V. Selinger, *Introduction to the Theory of Soft Matter: From Ideal Gases to Liquid Crystals* (Springer International, Cham, Switzerland, 2016).
- [51] A. L. Bernard, M.-A. Guedeau-Boudeville, V. Marchi-Artzner, T. Gulik-Krzywicki, J.-M. D. Meglio, and L. Jullien, Shear-induced permeation and fusion of lipid vesicles, *J. Colloid Interface Sci.* **287**, 298 (2005).
- [52] Y.-I. Cho and D. J. Cho, Hemorheology and microvascular disorders, *Korean Circ. J.* **41**, 287 (2011).
- [53] A. Rahimian, S. K. Veerapaneni, and G. Biroso, Dynamic simulation of locally inextensible vesicles suspended in an arbitrary two-dimensional domain, a boundary integral method, *J. Comput. Phys.* **229**, 6466 (2010).
- [54] A. Nait-Ouhra, A. Farutin, H. Ez-zahraouy, A. Benyoussef, and C. Misbah, Rheology of a confined vesicle suspension, *Phys. Rev. Fluids* **4**, 103602 (2019).
- [55] C. P. Moore, J. Husson, A. Boudaoud, G. Amselem, and C. N. Baroud, Clogging of a Rectangular Slit by a Spherical Soft Particle, *Phys. Rev. Lett.* **130**, 064001 (2023).
- [56] R.-J. C. Merath and U. Seifert, Fluctuation spectra of free and supported membrane pairs, *Eur. Phys. J. E* **23**, 103 (2007).
- [57] H. A. Faizi, C. J. Reeves, V. N. Georgiev, P. M. Vlahovska, and R. Dimova, Fluctuation spectroscopy of giant unilamellar vesicles using confocal and phase contrast microscopy, *Soft Matter* **16**, 8996 (2020).
- [58] V. Doyeux, S. Priem, L. Jibuti, A. Farutin, M. Ismail, and P. Peyla, Effective viscosity of two-dimensional suspensions: Confinement effects, *Phys. Rev. Fluids* **1**, 043301 (2016).
- [59] B. M. Haines and A. L. Mazzucato, A proof of Einstein's effective viscosity for a dilute suspension of spheres, *SIAM J. Math. Anal.* **44**, 2120 (2012).
- [60] A. S. Khair, The 'Einstein correction' to the bulk viscosity in n dimensions, *J. Colloid Interface Sci.* **302**, 702 (2006).
- [61] J. F. Brady, The Einstein viscosity correction in n dimensions, *Int. J. Multiphase Flow* **10**, 113 (1983).
- [62] B. J. Konijn, O. Sanderink, and N. P. Kruyt, Experimental study of the viscosity of suspensions: Effect of solid fraction, particle size and suspending liquid, *Powder Technol.* **266**, 61 (2014).
- [63] É. Guazzelli and O. Pouliquen, Rheology of dense granular suspensions, *J. Fluid Mech.* **852**, P1 (2018).
- [64] J. J. J. Gillissen, A. Papadopolou, S. Balabani, M. K. Tiwari, and H. J. Wilson, Suspension rheology of adhesive particles at high shear-rates, *Phys. Rev. Fluids* **5**, 053302 (2020).
- [65] O. Aouane, A. Scagliarini, and J. Harting, Structure and rheology of suspensions of spherical strain-hardening capsules, *J. Fluid Mech.* **911**, A11 (2021).
- [66] P. K. Singeetham, K. V. S. Chaithanya, and S. P. Thampi, Dilute dispersion of compound particles: deformation dynamics and rheology, *J. Fluid Mech.* **917**, A2 (2021).
- [67] A. Singh, G. L. Jackson, M. van der Naald, J. J. de Pablo, and H. M. Jaeger, Stress-activated constraints in dense suspension rheology, *Phys. Rev. Fluids* **7**, 054302 (2022).
- [68] D. Saintillan, Extensional rheology of active suspensions, *Phys. Rev. E* **81**, 056307 (2010).

- [69] T. Ishikawa, D. Brumley, and T. Pedley, Rheology of a concentrated suspension of spherical squirmers: monolayer in simple shear flow, *J. Fluid Mech.* **914**, A26 (2021).
- [70] A. McGlasson and L. C. Bradley, Investigating time-dependent active motion of Janus micromotors using dynamic light scattering, *Small* **17**, 2104926 (2021).
- [71] S. A. Mallory, F. Alarcon, A. Cacciuto, and C. Valeriani, Self-assembly of active amphiphilic Janus particles, *New J. Phys.* **19**, 125014 (2017).